J W S Cook

Doublet splitting and linear amplitude characteristics of alpha-particle driven ion cyclotron emission

Doublet splitting and linear amplitude characteristics of alpha-particle driven ion cyclotron emission

J W S Cook

Doublet splitting and linear amplitude characteristics of fusion alpha-particle driven ion cyclotron emission

J. W. S. Cook

UKAEA-CCFE, Culham Science Centre, Abingdon, OX14 3DB, UK

E-mail: `james.cook@ukaea.uk`

Jan 2022

Abstract. Ion cyclotron emission (ICE) originating from confined populations of fast ions in toroidal fusion plasmas is an important non-invasive, passive diagnostic for current and next generation devices. The ability to model the ICE signals accurately is an essential step towards inferring the characteristics of confined energetic alpha-particles or fast NBI ions and background plasma. In this paper, the linear growth rates of the magnetoacoustic cyclotron instability, which is the leading explanation for ICE, are calculated in high resolution 2D $(k_\perp, k_\parallel)$ space for parameters corresponding to JET Pulse No. 26148. These calculations shed further light on the origin of doublet-splitting of the cyclotron harmonics as well as the apparent need to invoke nonlinear interactions with 1D3V particle-in-cell studies to account for lower harmonics with substantial amplitudes: the inclusion of signals of ICE from a well resolved range of propagation angles can also account for these effects.

1. Introduction

Observations of ion cyclotron emission (ICE) have been reported from magnetically confined plasmas first in TFTR[1, 2] and JET[3, 4, 2], followed by other tokamaks PDX[5], JT-60-U[6], DIII-D[7], ASDEX[8], ASDEX-Upgrade[9], EAST[10], and KSTAR[11, 12]. Stellarators[13] and FRCs[14] have also exhibited this phenomenon. Energetic ion populations that give rise to ICE have their origins in fusion reactions in DT plasmas[15, 1], ICRH[15], and neutral beam injection[9]. ICE arising from fusion α-particles is a proposed route to further the understanding of burning plasmas in ITER[16, 17].

The foremost explanation of the mechanism responsible for ICE is the magnetoacoustic cyclotron instability (MCI)[18], which arises from the free energy present in energetic ions with inverted distributions in velocity space. Theoretical understanding of ICE is based in analytical solutions to the linearised Maxwell-Vlasov system of equations[19] where the energetic ion species was modelled as ring-beam for which $f(v_\parallel, v_\perp) \propto \exp(-(v_\parallel - u_\parallel)^2/v_{th}^2)\delta(v_\perp - u_\perp)$ [20, 21]. Here $u_\parallel$, $u_\perp$ and v_{th}

are the beam velocity (the signed drift speed along the magnetic field), ring speed (the speed perpendicular to the magnetic field) and thermal velocity, respectively. Subsequent studies augmented this understanding via nonlinear fully-kinetic[22, 11] and hybrid[23, 24] particle-in-cell (PIC) simulations in one dimension and 3 vector components for velocities and electromagnetic field (i.e. 1D3V), and recently 2D3V hybrid-PIC simulations[25]. These computational approaches also operate under the simplification that the plasma is both homogeneous and infinite albeit approximately via periodic boundary conditions. Linearised fluid approaches that incorporate toroidal geometry and inhomogeneous plasma and magnetic fields have shed light of the eigenmode structure of compressional Alfvén eigenmodes, which like ICE are also fast Alfvén modes driven by energetic ions, in spherical tokamaks[26, 27] and conventional aspect ratio tokamaks [28, 29, 30].

The effectiveness of analytical theory to reproduce the observed cyclotron harmonic peaks in the fluctuations of the magnetic field was first explained somewhat by 1D PIC simulations. In these simulations the onset of nonlinearity appeared to imprint the amplitudes of each of the harmonics into the signal as they are at the end of the linear phase; each mode grows independently until growth is terminated for all modes when the fastest mode enters its nonlinear phase meaning that both the amount of free energy available for instability has decreased and that the unstable energy ion distribution function has been perturbed into a more stable state. Analysis shows that only higher cyclotron harmonics are destabilised[17] to the MCI, however observations clearly indicate power at theoretically stable lower harmonics[3]. In a further step towards accurate recreation of experimental observations, nonlinear phases of hybrid[23] and fully kinetic[22, 11] PIC simulations went on to show that wave-wave coupling was responsible for raising the amplitude of lower cyclotron harmonics. Most recently, hybrid 2D simulations have begun to shed light on the 2D3V dynamics of ICE[25].

To better enable ICE as a diagnostic for confined fast ions, it is necessary to further develop our understanding with a range of tools. In this work, I present the 2D $(k_\perp, k_\parallel)$ growth rates of the MCI under the conditions of outer mid-plane of the JET PTE[4] Pulse No. 26148. These growth rates are obtained from a dispersion relation solver, PlasmaDispersionRelations.jl, written in the Julia programming language[31]. These results narrow the gap between analytical theory and expensive HPC simulations and can be run readily on desktop computers in a matter of minutes, further enabling research into this topic. Note that this study focusses on edge-ICE, named for the region from which the signal arises, as opposed to core-ICE[9].

In section 2, the computational method is described for calculating the linear growth rates, which are presented for energetic ring-beam alpha-particles with non-zero perpendicular thermal spread in section 3. Results are summarised in section 4.

2. Computational method

Solutions to the linearised Maxwell-Vlasov system of equations are found in $(k_\parallel, k_\perp)$ space for a ring-beam distribution of energetic minority alpha-particles and Maxwellian electrons and background thermal majority deuteron ions. Calculations are made for alpha-particles with ring-beams of two values of pitch-angle cosine: $u_\parallel = -0.646u_0 \approx -\cos(\arcsin(\sqrt{R_0 \sin(\psi_0)/R_{ICE}})) \simeq -1.1V_A$, which is associated with the ion-cyclotron emission observed on JET Pulse No. 26148 for which $R_0 = 3.46$ m and $\psi_0 = 55.2°$ are the major radius and pitch angle at birth, and $R_{ICE} = 4$ m is the major radius of the emission region, see Figs. 3 and 14 and associated text in Ref. [4]; and $u_\parallel = 0u_0$ representing a ring distribution with no parallel drift, see Fig. 1(a) of Ref [22]. Here, V_A is the Alfvén speed and $u_0 = \sqrt{u_\parallel^2 + u_\perp^2}$ is the speed of an alpha-particle with an energy of 3.6 MeV. The complex frequency solutions, ω, along the fast Alfvén branch are found on a grid of $(k_\parallel, k_\perp)$.

The plasma parameters approximate those found in the region indicated in Fig. 3 of Ref. [4], which are associated with the continuous trace signal of Fig. 2 (ibid). The electrons and deuterons have temperatures of 1 keV and the electrons have a number density of 1.7×10^{19} m^{-3}. The magnetic field is 2.07 T, which corresponds a major radius of 4 m. The ring-beam distribution function, Eq. 3, is a separable function of the beam in $v_\parallel$ given by Eq. 1 and the ring in $v_\perp$ given by Eq. 2. This distribution function is parameterised by the drift velocity parallel to the magnetic field $u_\parallel$, the drift speed perpendicular to the magnetic field $u_\perp$, and the thermal velocity in both directions v_{th}. The thermal spread of the alpha particles' distribution function $v_{th} = v_{\parallel,th} = v_{\perp,th} = u_0/100$. The number density ratio of alpha-particles to deuterons is 1.5×10^{-4}.

$$f_{\alpha,\parallel}\left(v_\parallel\right) = \frac{\exp\left(-\frac{(v_\parallel - u_\parallel)^2}{v_{\parallel,th}^2}\right)}{v_{\parallel,th}\sqrt{2\pi}} \tag{1}$$

$$f_{\alpha,\perp}\left(v_\perp\right) = \frac{1}{2\pi} \frac{\exp\left(-\frac{(v_\perp - u_\perp)^2}{v_{\perp,th}^2}\right)}{\left(\frac{\sqrt{\pi}}{2}v_{\perp,th}u_\perp(1 - \mathrm{erf}(-\frac{u_\perp}{v_{\perp,th}})) + \exp(-u_\perp^2/v_{\perp,th}^2)\frac{v_{\perp,th}^2}{2}\right)} \tag{2}$$

$$f_\alpha\left(v_\parallel, v_\perp\right) = f_{\alpha,\parallel}\left(v_\parallel\right) f_{\alpha,\perp}\left(v_\perp\right) \tag{3}$$

Solutions to the linearised Maxwell-Vlasov system of equations are given by the dispersion relation, Eq. 4, which is satisfied for sets of $(\omega, \vec{k})$ given the distribution functions of all the species present. The hot dielectric tensor[19], $\vec{\overleftrightarrow{\epsilon}}$, Eq. 5 is calculated for each species.

$$0 = ||\vec{\epsilon} + \left(\vec{k} \otimes \vec{k} - \vec{I}(\vec{k} \cdot \vec{k})\right)\frac{c^2}{\omega^2}||, \tag{4}$$

$$\vec{\epsilon} = \vec{1} + \sum_s \frac{\Pi_s^2}{\omega} \sum_{n=-\infty}^{\infty} \int_0^{\infty} \int_{-\infty}^{\infty} \frac{\vec{S}_{s,n} 2\pi v_\perp dv_\perp dv_\parallel}{\omega - k_\parallel v_\parallel - n\Omega_s} \tag{5}$$

where

$$\vec{S}_{s,n} = \begin{bmatrix} \frac{n^2 J_n^2}{z_s^2} v_\perp U_s & \frac{in J_n J_n'}{z_s} v_\perp U_s & \frac{n J_n^2}{z_s} v_\perp W_{s,n} \\ \frac{-in J_n J_n'}{z_s} v_\perp U_s & (J_n')^2 v_\perp U_s & -i J_n J_n' v_\perp W_{s,n} \\ \frac{n J_n^2}{z_s} v_\parallel U_s & i J_n J_n' v_\parallel U_s & n J_n^2 v_\parallel W_{s,n} \end{bmatrix}, \tag{6}$$

$$U_s = \frac{\partial f_s}{\partial v_\perp} + \frac{k_\parallel}{\omega}\left(v_\perp \frac{\partial f_s}{\partial v_\parallel} - v_\parallel \frac{\partial f_s}{\partial v_\perp}\right), \tag{7}$$

$$W_{s,n} = \left(1 - \frac{n\Omega_s}{\omega}\right)\frac{\partial f_s}{\partial v_\parallel} + \frac{n\Omega v_\parallel}{\omega v_\perp}\frac{\partial f_s}{\partial v_\perp}, \tag{8}$$

J_n is the nth Bessel function of the first kind taking the argument $z_s = k_\perp v_\perp/\Omega_s$ and $J_n' = \frac{\partial J_n}{\partial z}$.

The integrals over perpendicular velocity required for calculating the dielectric tensor for Maxwellian distribution functions are given in terms of modified Bessel functions of the first kind[19] for both electrons and ldeuterons i.e. when $u_\perp = 0$. The same perpendicular integrals over the alpha-particles' ring distribution is calculated numerically via Gauss-Kronrod[33] quadrature using the GaussGK.jl[34] library. An absolute and relative tolerance of 0 and 10^{-8}, respectively, on the value of the integrals is used.

Since all the parallel distribution functions for all species are Maxwellians, the parallel integrals can be calculated from the well known plasma dispersion function[37], which is laid out in the appendix.

The summation over Bessel function indices in Eq. 5 continues until the relative change of the L2 norm between the current and previous iteration is less than a tolerance of 10^{-8}. Root finding of Eq. 4 is performed by an amalgamation of the Nelder-Mead[35] optimisation method with the winding number method, whereby if the Nelder-Mead simplex does not contain a root, as calculated via the winding method, then the optimisation procedure follows the Nelder-Mead method, otherwise a non-zero winding number indicates that a root is present within the simplex and the simplex bifurcates. The child simplex that contains the root is used for the next iteration. The optimisation iteration procedure finishes when the real extent of the simplex is less than $10^{-4}\,\Omega_i$ and the imaginary extent is less than $10^{-5}\,\Omega_i$, where Ω_i is the cyclotron frequency of both the alpha-particles and deuterons since they share a charge-mass ratio. This approach is found to be adequately robust and faster than the Nelder-Mead method or winding number approach used in isolation of one another. Each 512 by 512 scan in $(k_\perp, k_\parallel)$ takes between 5 and 6 minutes on a laptop.

3. Linear growth rates

The growth rates of unstable modes for the case where the pitch-angle cosine value is zero ($u_\parallel = 0$ in Eq. 1) are plotted in Fig. 1(a) against the associated real frequency (only modes with growth rates in excess of the solver tolerance are shown i.e. $\Im(\omega) > 10^{-5}\Omega_i$). In this panel shading indicates parallel wavenumber in units of Ω_i/V_A. Fig. 1(b) plots the same data in the $(\omega, k_\parallel)$ plane where shading instead indicates growth rates. The simplicity of the consecutive unstable cyclotron harmonics visible in panel (a) betrays the complexity of the structure in the $(\omega, k_\parallel)$ plane. Integration over $k_\parallel$ projects the solutions onto the frequency axis, which loses the structure and produces narrow harmonics. Figure 2 shows the same data as Fig. 1 in $(k_\perp, k_\parallel)$ space with damped and normal modes in addition, except shading indicates the growth rates. Overlaid contours indicate the real frequency in units of ion cyclotron harmonics. Only narrow regions around the cyclotron harmonics are unstable. Overlaid straight traces indicate propagation angle. No Doppler shift is present due to the lack of parallel drift in the alpha-particle ring-beam. The growth rate increases approximately linearly with cyclotron harmonic number, which is consistent with the literature[20]. Together these figures serve to introduce a 2D view (growth rates in $(k_\perp, k_\parallel)$ space) of traditionally 1D data (growth rates against frequency). This will become important when a non-zero $u_\parallel$ is taken into account next.

Fig. 3 plots solutions for the physically more realistic pitch-angle case ($u_\parallel = -0.646u_0$) in the same manner as Fig. 1. There are several points worth noting. First, the growth rate is no longer linear with cyclotron harmonic number. Second, harmonics are broader due to the non-zero parallel drift that gives rise to strong Doppler shift with increasing $|k_\parallel|$. Third, doublet splitting of the 10th and 11th harmonics is observed: see Fig. 2 of Cottrell 1993 for a single signal showing multiple doublet splittings; Fig. 3 of Dendy et al 1994 (also Fig. 9 Dendy et al 1995) shows slices at constant propagation angle that when all superimposed point towards doublet splitting, albeit under-resolved in wavenumber space. The following describes how these three features are connected. Doublet splitting arises due to the dip in growth rate along the band of instability where $k_\parallel$ goes through zero combined with the change in sign of the Doppler shift of the real frequency as $k_\parallel$ changes sign. The effect is larger for higher harmonics where the growth rate diminishes to zero for perpendicular propagation; see e.g. the 12th harmonic in Fig. 4 near ($k_\parallel \simeq 0$ $\Omega_i/V_A, k_\perp \simeq 13$ Ω_i/V_A), where V_A is the Alfvén speed. Other possible mechanisms for doublet splitting could be grad-B or curvature drifts[4, 36]. Qualitatively, Fig. 3(a) resembles Fig. 2 of Cottrell 1993 in that the signal below the 7th cyclotron harmonics is lower and flatter with well defined peaks and the signal beyond the 7th harmonic is a step-change larger and the harmonics are less easily identifiable. These features cannot be be recreated with a 1D calculation for these distributions functions. Note that Fig. 4 shows these two different regimes more clearly. The lower frequency behaviour, where $k_\perp < 7\Omega_i/V_A$, is characterised by narrow regions of instability near Doppler shifted cyclotron harmonics that are stabilised when
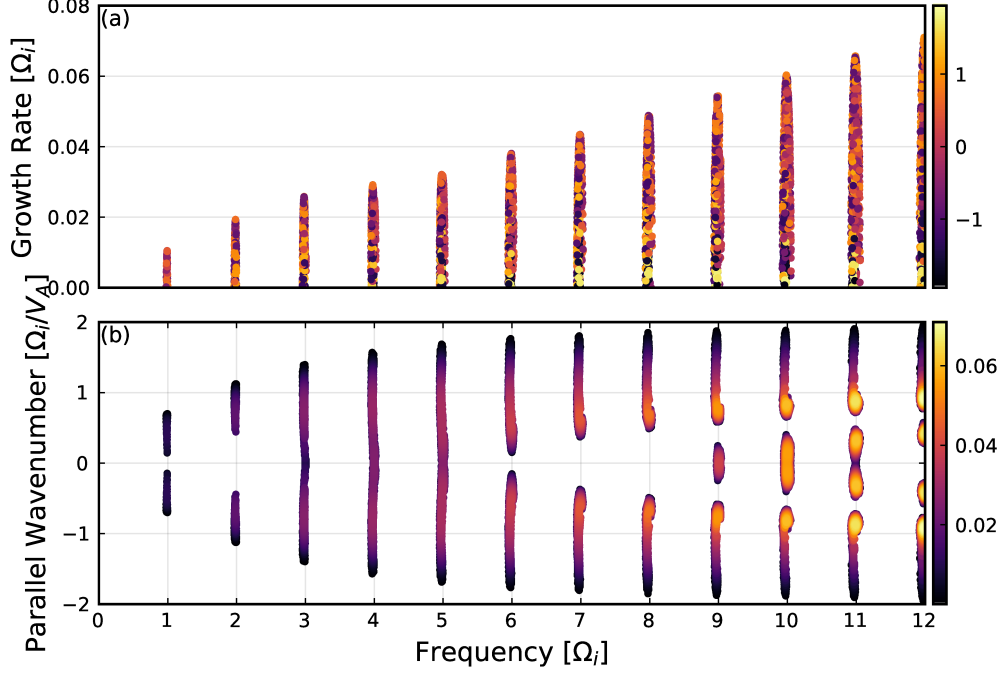
Figure 1. (colour online) Unstable fast Alfvén wave solutions to the linear Maxwell-Vlasov system of equations, Eq. 4, for thermal electrons, deuterons and a ring distribution of energetic alpha-particles i.e. when there is zero parallel drift, $u_\parallel = 0$ in Eq. 1. (a) Upper panel: growth rate as a function of real frequency where shading indicates the parallel wavenumber, $k_\parallel$, in units of Ω_i/V_A of the complex frequency solution. Consecutive cyclotron harmonics are increasingly unstable and are narrow due to the lack of Doppler shift associated with parallel drifts. (b) Lower panel: the same solutions as in panel (a) in the $(\omega, k_\parallel)$ plane where shading indicates growth rate. The complex structure of the growth rates that exists in wavenumber space is projected into sharp harmonics on the frequency axis.

$k_\parallel = 0$ but unstable at larger negative parallel wavenumbers. The higher frequency behaviour in the region $\omega \geq 7\Omega_i$ is dominated by broader regions of instability in frequency and wavenumber near to Doppler shifted cyclotron harmonics, which have a complex structure in wavenumber space. Modes numbering 1, 2, 6, 7, 8, 12, and 13 are stable when propagating exactly perpendicular whilst obliquely propagating modes remain unstable; see Fig. 9 of Dendy et al 1995, which plots the analytic expression for the growth rate of the MCI at 5 slices of propagation angle. The Doppler shift of the growing modes can reach $\approx \Omega_i$ for large propagation angles at lower frequencies and also for oblique angles at higher frequencies; see, for example, the mode associated with the 15th cyclotron harmonic near $k_\parallel \simeq -\frac{3}{4}\Omega_i/V_A, k_\perp \simeq 14\Omega_i/V_A$, i.e. a propagation angle of 93°. Furthermore, the breadth of the harmonics can be attributed to the contributions from multiple propagation angles even though the lower harmonics are largely stable for forward travelling and perpendicular propagation angles.
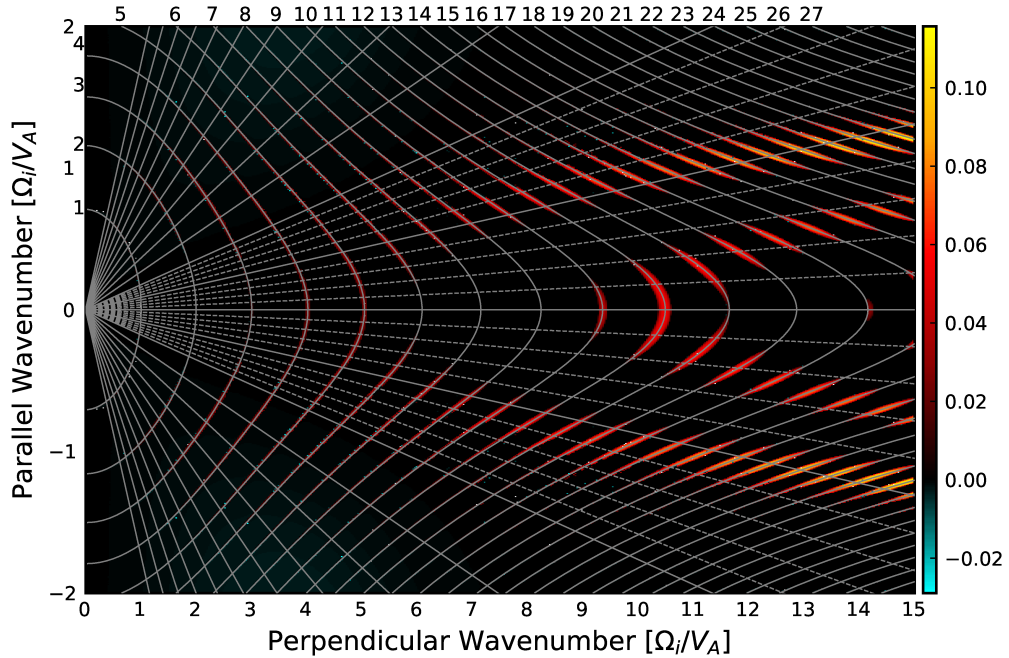
Figure 2. (colour online) Shading indicates the growth rate of fast Alfvén waves excited by a ring of fusion born alpha-particles, as a function of parallel wavenumber on the ordinate and perpendicular wavenumber on the abscissa. No solution is found where shading is absent. The alpha-particle distribution function is given by Eq. 3 with $u_\parallel = 0$. Consecutive straight traces indicate the propagation angle with respect to the magnetic field: the horizontal line is exactly perpendicular; solid traces fan out at intervals of five degrees; and dashed traces indicate intervals of one degree. Curved grey traces indicate the location in $(k_\perp, k_\parallel)$ of the cyclotron harmonics (i.e. the real component of the complex ω solutions), which are annotated along the left hand side and upper edge of the figure. Frequencies are in units of the alpha-particle cyclotron frequency, and wavenumbers are in alpha-particle cyclotron frequencies per Alfvén speed. Note the up-down symmetry due to the lack of parallel drift in the energetic alpha particles.

4. Summary

This paper presents the linear Maxwell-Vlasov dispersion relation of a plasma consisting of thermal electrons, thermal deuteron fuel ions and a minority energetic ring-beam of fusion born alpha-particles. These high resolution $(k_\perp, k_\parallel)$ calculations revisit ICE observations from JET Pulse No. 26148[4, 2] and reproduce several important features: the step change in signal strength from $\omega < 6$ to $\omega > 6$; the doublet splitting of peaks at $\omega \approx 10\Omega_i$ in Fig. 3, with origins visible in the fine $(k_\parallel, k_\perp)$ structure in Fig. 4. The Doppler shift for large $k_\parallel$ becomes of the order of the alpha-particle cyclotron frequency, which makes it difficult to determine which parts of the signal come from which cyclotron harmonic numbers. Further effort is required to account for the extra doublets visible in the continuous trace associated with JET Pulse No. 26148 in Fig. 2 of Ref. [4].

These calculations capture the finite perpendicular thermal spread of the alpha
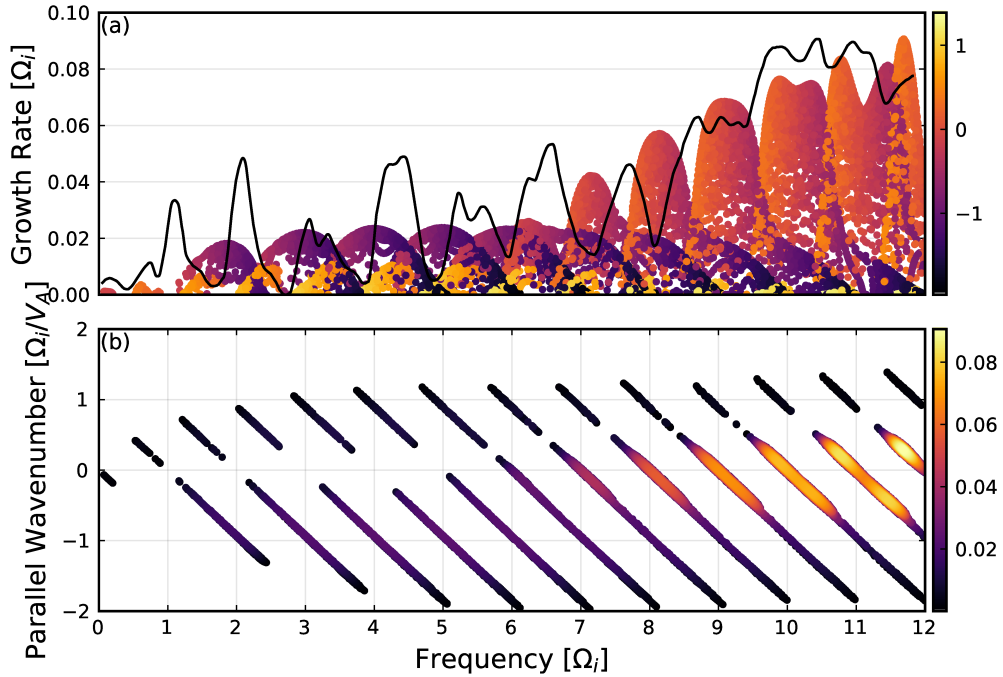
Figure 3. (colour online) The imaginary component of the frequencies for the case with parallel drift $u_\parallel = -0.646u_0 \simeq -1.1V_A$. Panel (a) plots growth rate against frequency where shading indicates parallel wavenumber in units of Ω_i/V_A, and (b) plots the solutions in the $(\omega, k_\parallel)$ plane where shading indicates growth rate. Note that the Doppler shift associated with the non-zero parallel drift speed broadens the unstable peaks in frequency. The 10th and 11th cyclotron harmonics are split into doublets, i.e. they have two peaks. Compare with Fig. 2 of Cottrel et al 1993.

particle distribution function, the integral of which has no known analytically tractable form. The computational capabilities of the software, PlasmaDispersionRelations.jl, used to generate the results further enable ICE as a diagnostic for fusion plasmas since the code is capable of: calculating the dispersion relation of plasmas consisting of an arbitrary number of species; and of arbitrary distribution functions, although those with parallel Maxwellians, like those presented here, are faster. It has been shown that it is possible to qualitatively recreate signals containing lower harmonics of substantial amplitudes by invoking 2D linear physics. The presence of ICE signals at lower harmonics in PIC simulations has been attributed to nonlinear interactions between pairs of more powerful higher harmonics[23]. This work suggests that observations of lower ICE harmonics may arise either due to the effects of 2D linear physics or to nonlinear 1D physics[12], or a combination. There are several important features missing from these calculations. Among them are the effects of the spatial inhomogeniety of the magnetic field and background plasma, and the quantisation associatied with toroidal periodicity. These effects may create an eigenmode structure, not accounted for herein, associated with the kinetic MCI. Cottrell et al. [4] does discuss the implications of propagation angles on ICE signals and indicate that lower harmonics must propagate
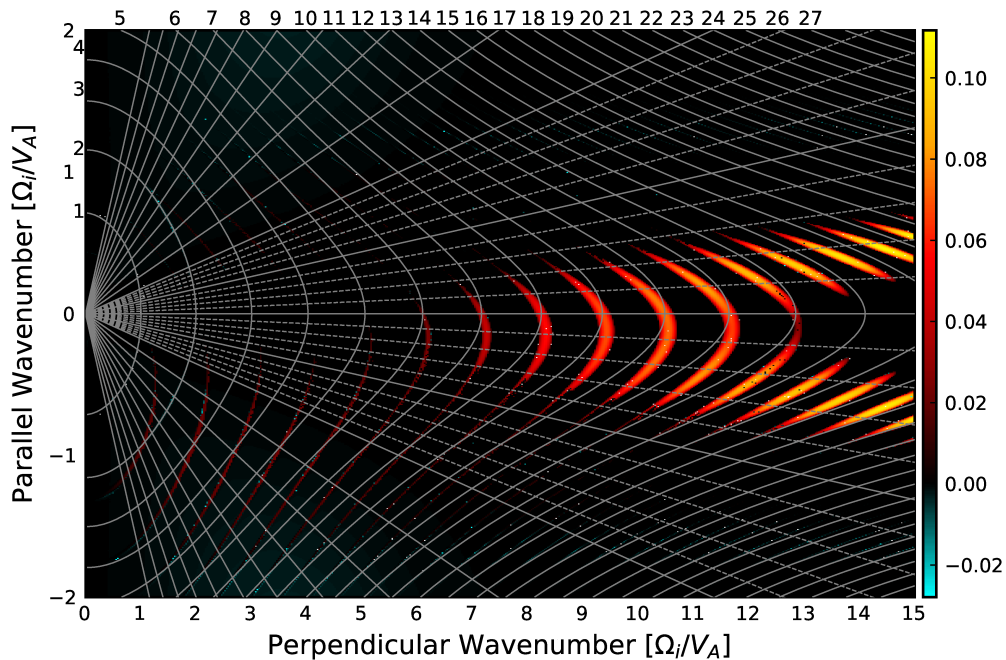
Figure 4. (colour online) As in Fig. 2, except for a ring-beam of alpha particles with a more realistic pitch-angle value $u_\parallel = -0.646u_0 \simeq -1.1V_A$. The non-zero parallel drift speed causes up-down asymmetry; this figure for a pitch-angle cosine of the opposite sign, $u_\parallel = 0.646u_0$, is identical expect flipped about $k_\parallel = 0$.

increasingly close to exactly perpendicular. These effects remain the subject of further work to incorporate them in linear and nonlinear studies of ICE.

This work showcases a new high resolution tool for studying ICE and captures the fine detail of ICE signals, which is challenging to capture with nonlinear PIC code simulations since they suffer from low resolution in frequency and wavenumber space due to the phenomenon's transience and computational expense, respectively. As such, this work represents a complementary tool that builds upon purely analytical work and nonlinear PIC studies, which in turn enhances the feasibility of exploiting ICE as a passive diagnostic of confined and leaving ions in magnetised fusion plasmas.

5. Acknowledgements

It is a pleasure to thank R O Dendy and B Chapman-Oplopoiou for useful discussions.

Appendix A.

The plasma dispersion function[37]

$$Z_n(z) = \frac{1}{\sqrt{\pi}} \int_{-\infty}^{\infty} \frac{x^n e^{-x^2}}{x - z} dx, \tag{A.1}$$
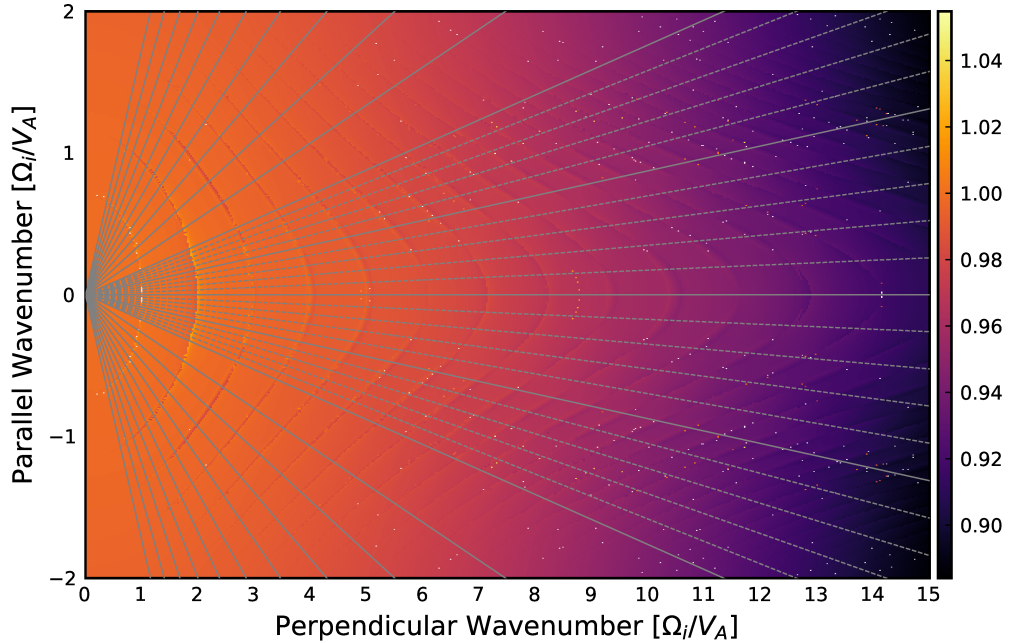
Figure 5. (colour online) As in Fig. 2, except that the shading indicates the real part of the smoothed solution normalised by the high frequency expression for the fast Alfvén wave set out in Eq. 25 of Ref. [20], which is also Eq. 11 in Ref. [21]. The differences in real frequency for the two sets of calculations, a pitch-angle cosine of -0.646 and zero, are negligible.

can be calculated via the recurrence relation[38]

$$Z_n(z) = zZ_{n-1}(z) + \begin{cases} 0 & \text{if } n \in \{2k : k \in \mathbb{Z}\} \\ 1 & \text{if } n = 1 \\ \frac{1}{2} & \text{if } n = 3 \\ 2^{\frac{1-n}{2}} \Pi_{i=1}^{\frac{n-3}{2}} (2i+1) & \text{otherwise,} \end{cases} \qquad (A.2)$$

where $n \geq 0$ and the cases $n = 1$ and $n = 3$ are stated explicitly to avoid confusion. The zeroth term is defined as

$$Z_0(z) = i\sqrt{\pi}\text{erfcx}\left(-iz\right) \qquad (A.3)$$

where erfcx is the scaled complementary complex error function.

[1] Cauffman S, Majeski R, McClements K G, and Dendy R O 1995 *Nucl. Fusion* **35** 1597

[2] Dendy R O, McClements K G, Lashmore-Davies C, Cottrell G A, Majeski R, and Cauffman S 1995 *Nucl. Fusion* **35** 1733–1742

[3] Cottrell G A and Dendy R O 1988 *Phys. Rev. Lett.* **60** 33-6

[4] Cottrell G A, Bhatnagar V, Costa O D, Dendy R O, Jacquinot J, McClements K G, McCune D, Nave M, Smeulders P, and Start D 1993 *Nucl. Fusion* **33**, 31365–1387

[5] Heidbrink W and Sadler G 1994 *Nucl. Fusion* **34** 535–615

[6] Ichimura M, Higaki H, Kakimoto S, Yamaguchi Y, Nemoto K, Katano M, Ishikawa M, Moriyama S, and Suzuki T 2008 *Nucl. Fusion* **48**, 035012

[7] Heidbrink W W et al 2011 *Plasma Phys. Control. Fusion* **53** 085028

[8] D'Inca R 2014 *Ion Cyclotron Emission on ASDEX Upgrade PhD Thesis* Ludwig-Maximilians-Universitat

[9] Ochoukov R et al 2018 *Rev. Sci. Instrum.* 2018 **89**, 10J101

[10] Liu L et al 2020 *Nucl. Fusion* **60** 044002

[11] Chapman B, Dendy R O, McClements K, Chapman S C, Yun G, Thatipamula S, and Kim M 2017 *Nucl. Fusion* **57** 124004

[12] Chapman B, Dendy R O, Chapman S C, McClements K G, Yun G S and Thatipamula S G 2018 *Nucl. Fusion* **58** 096027

[13] Saito K et al 2013 *Plasma Sci. Technol.* **15** 209–212

[14] Nicks B S, Magee R, Necas A and Tajima T 2021 *Nucl. Fusion* **61** 016004

[15] Cottrell G A 2000 *Phys. Rev. Lett.* **84** 2397-400

[16] Dendy R O and McClements K G 2015 *Plasma Physics and Controlled Fusion* **57** 044002

[17] McClements K G, Dendy R O 2015 *Nucl. Fusion* **55** 043013

[18] Belikov V S and Kolesnichenko Ya I 1976 *Sov. Phys. Tech. Phys.* **20** 1146

[19] Stix T H 1992 *Waves in Plasmas. 2nd Edition* (Springer, New York)

[20] Dendy R O, Lashmore-Davies C N, McClements K G and Cottrell G A 1994 *Physics of Plasmas* **1** 1918-28

[21] McClements K G, Dendy R O, Lashmore-Davies C N, Cottrell G A, Cauffman S and Majeski R (1996) *Phys. Plasmas* **3** 543

[22] Cook J W S, Dendy R O, Chapman S C 2013 *Plasma Physics and Controlled Fusion* **55** 065003

[23] Carbajal L, Dendy R O, Chapman S C, and Cook J W S 2014 *Phys. Plasmas* **21** 012106

[24] Reman B, Dendy R O, Akiyama T, Chapman S C, Cook J W S, Igami H, Inagaki S, Saito K, and Yun G, 2019 *Nucl. Fusion* **59** 096013

[25] Carbajal L, and Calderón F A 2021 *Phys. Plasmas* **28** 014505

[26] Sharapov S E , Lilley M K, Akers R, Ayed N B, Cecconello M, Cook J W S, Cunningham G, and Verwichte E 2014 *Phys. Plasmas* **21** 082501

[27] Gorelenkov N N 2016 *New J. Phys.* **18** 105010

[28] Kolesnichenkoo Ya I, Fülöp T, Lisak M and Anderson D 1998 *Nucl. Fusion* **3**8 1871

[29] Fülöp T, Lisak M, Kolesnichenko Ya I, and Anderson D, 2000 *Phys. Plasmas* **7** 1479–1486

[30] Heidbrink W W, Fredrickson E, Gorelenkov N N, Rhodes T, Zeeland M A 2006 *Nucl. Fusion* **46** 324

[31] Bezanson J, Edelman A, Karpinski S, and Shah V B 2017 *SIAM review* **59** 1

[32] Fredrickson E D, Gorelenkov N N, Bell R E, Diallo A, LeBlanc B P, Podestà M, and NSTX Team 2019 *Physics of Plasmas* **26**, 032111

[33] Kronrod A S 1965 *Nodes and weights of quadrature formulas. Sixteen-place tables* (New York: Consultants Bureau (Authorized translation from the Russian))

[34] Johnson S G *QuadGK.jl: Gauss-Kronrod integration in Julia* https://github.com/JuliaMath/QuadGK.jl

[35] Nelder J A and Mead R 1965 *Computer Journal* **7** 4

[36] Fülöp T and Lisak M 1998 *Nucl. Fusion* **38** 761

[37] Fried B D and Conte S C 1961 *The Plasma Dispersion Function* (Academic Press, New York)

[38] Sampoorna M, Nagendraa K N, Frisch H 2007 *Journal of Quantitative Spectroscopy & Radiative Transfer* **104** 71-85